

High-temperature oxidation behavior of 9Cr-5Si-3Al ferritic heat-resistant steel

Jun-jun Yan, Xue-fei Huang, Wei-gang Huang*

College of Materials Science and Engineering, Sichuan University, Chengdu 610065, China

Abstract: To improve the oxidation properties of ferritic heat-resistant steels, in this study, we designed an Al-bearing Fe-9Cr-5Si-3Al ferritic heat-resistant steel. We then conducted cyclic oxidation tests to investigate the high-temperature oxidation behavior of Fe-9Cr-5Si and Fe-9Cr-5Si-3Al ferritic heat-resistant steels at 900°C and 1000°C. The characteristics of the oxide layer were analyzed by X-ray diffraction, scanning electron microscopy, and energy dispersive spectroscopy. The results show that the oxidation-kinetics curves of the two tested steels follow the parabolic law, with the parabolic rate constant K_p of Fe-9Cr-5Si-3Al steel being much lower than that of 9Cr-5Si steel at both 900°C and 1000°C. The oxide film on the surface of the 9Cr-5Si alloy exhibits Cr_2MnO_4 and Cr_2O_3 phases in the inner layer after oxidation at 900 °C and 1000°C. However, at oxidation temperatures of 900°C and 1000°C, the oxide film of the 9Cr-5Si-3Al alloy consists only of Al_2O_3 and its oxide layer is thinner than that of the 9Cr-5Si alloy. These results indicate that the addition of Al to Fe-9Cr-5Si steel can improve its high-temperature oxidation resistance, which can be attributed to the formation of a continuous and compact Al_2O_3 film on the surface of the steel.

Keywords: Ferritic heat-resistant steel, High-temperature oxidation, Oxidation kinetics, Aluminum

1 Introduction

Due to their high-temperature strength and high-temperature oxidation resistance, heat-resistant steels are widely used in equipment that must be operated in high-temperature environments, such as boiler pipelines, steam headers, steam lines, and other parts used in ultra-supercritical power plants, automotive exhaust systems, and solid oxide fuel cells [1-4]. Among the heat-resistant steels, ferritic heat-resistant steels have attracted much interest due to their good corrosion resistance, excellent thermal properties, and mechanical strength. In addition, the price of these steels is very competitive in comparison to austenitic heat-resistant steels containing high Cr and Ni.

One important ferrite heat-resistant steel, 9–12%Cr martensitic-ferritic steel, has high creep resistance, good oxidation resistance, and high-temperature strength and has been used in the construction of boilers parts and steam pipes in ultra-supercritical power plants and nuclear power plants [5-9]. To improve creep strength, Mo, W, V, Nb and other alloying elements have been used in 9–12 ferritic heat-resistant steels via solid-solution strengthening and precipitation hardening [10, 11]. Zhou et al. reported that the refinement of martensitic laths and second-phase particles improves high-temperature performance due to the lack of coarse $M_{23}C_6$ carbide and Laves phases [8, 10]. Fe-based oxide-dispersion-strengthened steels with yttria and Al have been reported to exhibit good high creep resistance and superior corrosion resistance

[10, 12].

Ferritic heat-resistant stainless steel, another ferritic heat-resistant steel with high-temperature performance and corrosion resistance, is resistant to higher temperatures than 9–12% Cr martensitic-ferritic steel due its more than 15% Cr concentration [13-15]. Homogeneous shear deformation and uniform recrystallized grains with random orientations have been reported to be obtainable by the use of an asymmetric rolling process as a heavy plastic deformation method to achieve asymmetric grains that are ultra-fine in size [16].

High-temperature oxidation resistance is considered to be an important property of ferritic heat-resistant steel. Although the structure of oxide films is complex in different steels due to the different types and contents of the alloying elements, much work on oxidation at high temperature has been conducted in recent years [4, 13, 17, 18]. Cr plays a dominant role in high-temperature oxidation, which can be attributed to the formation of protective Cr_2O_3 scales on the surface of the matrix that act as a barrier to the diffusion of oxygen through the oxide film, which would lead to the further oxidation of the matrix. However, since a higher Cr content can result in phase instability, to further hinder the internal diffusion of oxygen, the addition of Mn yields the more stable manganese spinel Cr_2MnO_4 on the surface of the matrix than can be obtained with just Cr_2O_3 [13, 19, 20]. Zhou et al. reported that a $(\text{Fe, Cr})_2\text{O}_3$ phase forms on the surface of 9% Cr ferritic heat-resistant steel oxidized at 700°C [7]. As an element with a high affinity for oxygen, Al is the main alloy used to improve oxidation resistance by the formation of Al_2O_3 on the surface of steels, with a single

Al₂O₃ phase occurring on the outer layer of this oxide film [13, 14, 17].

The great increase in municipal solid waste presents a serious problem as the population continues to increase along with ongoing economic development. Among the municipal solid-waste disposal options, waste incineration is an effective technology that can reduce the volume of solid waste by 90%. Currently, grate-firing technology is commonly used for waste incineration [21-23]. However, superalloys such as Inconel 718 and Inconel 600, which are generally used in waste incinerators, greatly increase the cost of this operation. Therefore, in this study, we designed the Fe-9Cr-5Si-3Al ferritic heat-resistant steel and conducted a detailed investigation of the high-temperature oxidation behavior of steels containing Al.

2 Materials and Methods

In this experiment, we used 9Cr-5Si and 9Cr-5Si-3Al ferritic heat-resistant steels, the chemical compositions of which are shown in Table 1. First, the steels were melted in a vacuum induction furnace, whereby the ingots were homogenized at 1200°C for 180min and then hot-forged into billets with dimensions of 25mm × 65mm × 800mm. For the oxidation tests, rectangular specimens were cut from the forged billets to the dimensions 15mm × 10mm × 5mm using an electrical discharge machine. Prior to the oxidation tests, the surfaces of all the specimens were mechanically ground with abrasive paper with grit numbers up to 1500 (10µm SiC particles) and then polished, degreased in an acetone bath, and cleaned ultrasonically in an ethanol bath.

Cyclic oxidation tests were performed at 900°C and 1000°C in a box-type electric-resistance heating furnace (type: SX2-10-13, Shanghai, China) for oxidation times of 10h, 30h, 50h, 70h, and 90h. Corundum crucibles were prepared and baked in a resistance heating furnace at 1100°C for 2h to remove any residues inside the corundum crucibles and thus ensure the constant weight of the crucibles. Before each oxidation test, a crucible containing one specimen was baked at 120°C for 1h. The total weight of the specimen and crucible was determined before and after the oxidation tests using an electronic balance (type: TE124S) with a resolution of 10^{-4} g.

We analyzed the phases of the oxide scale on the oxidized sample surface by X-ray diffraction (XRD) (40kV, 40mA, and Cu $K_{\alpha 1}$, $\lambda = 1.54056\text{\AA}$). We investigated the surface morphology and cross-section of the oxide scale on the sample surface using a scanning electron microscope (SEM, S-3400N) equipped with an electron dispersive spectroscope (EDS). We also determined the chemical composition of the oxide scale using EDS.

To protect the oxide scales and facilitate their observation, we deposited a layer of gold onto the oxide layer by vapor deposition.

Table 1. Chemical composition of the tested steels (wt%)

Alloy	Al	C	Si	Mn	P	S	Cr	Nb	Fe
9Cr-5Si	-	0.27	5.6	0.36	0.0072	0.0045	9.12	0.290	bal
9Cr-5Si-3Al	2.90	0.28	5.5	0.32	0.0088	0.0048	9.07	0.298	bal

3 Results and Discussion

3.1. Cyclic oxidation kinetics

Fig. 1 shows the cyclic oxidation-kinetics curves of the 9Cr-5Si and 9Cr-5Si-3Al ferritic heat-resistant steels at 900°C and 1000°C. In the figure, we can see that the weight gain per unit area increases with increases in the oxidation time for a given oxidation temperature. We can also see that, for both alloys, the weight gain increases with an increase in the oxidation temperature. The total weight gains at the end of the cycles up to 90h at 900°C and 1000°C for the 9Cr-5Si and 9Cr-5Si-3Al alloys are 0.508mg/cm², 0.197mg/cm² and 1.831mg/cm², 0.318mg/cm², respectively. Furthermore, the oxidation rate of the 9Cr-5Si alloy at 1000°C is much higher than that at 900°C. As a result, the weight gain of the 9Cr-5Si alloy is significantly greater by about 72.2% when the oxidation temperature was increased from 900°C to 1000°C. The 9Cr-5Si-3Al alloy, however, exhibits no significant increase in weight gain as the oxidation temperature increased from 900°C to 1000°C. As evident from Fig. 1, the oxidation rate of the 9Cr-5Si-3Al alloys is low and remains constant after about 30h, which indicates that the addition of Al can obviously improve the oxidation resistance of the alloy, especially at a higher temperature.

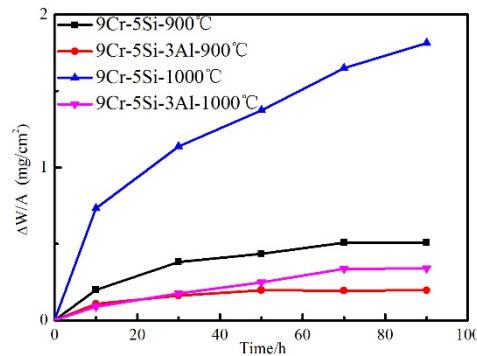


Fig. 1. Cyclic oxidation-kinetics curves of two samples oxidized in air at 900 °C and 1000 °C

As shown in Fig. 1, the cyclic oxidation-kinetics curves of the two kinds of alloys follow a parabolic rate law at oxidation temperatures of 900 °C and 1000°C. This means that a protective oxide layer forms during the first stage of oxidation and then the growth of this oxide layer is controlled by the diffusion of metal or oxygen during the oxidation process. As a result, the decrease in the weight gain in the subsequent oxidation process can be attributed to the lower diffusion coefficient of the elements in the oxide film formed on the surface.

The oxidation kinetics of the two alloys shown in Fig. 1 follow Equation (1) below [14], which indicates the relationship between the oxidation time t and weight gain per unit area of a sample, where k_p is a parabolic rate constant. A low k_p value indicates a low oxidation rate, that is, high oxidation resistance. Using Equation (1), we can fit a linear regression line of $(\frac{\Delta W}{A})^2$ versus t , as shown

$$(\Delta W/A)^2 = k_p \cdot t \quad (1)$$

in Fig. 2. This also confirms the parabolic features of the oxidation kinetics of the tested alloys. From Fig. 2, we can obtain the parabolic rate constant k_p values, which are listed in Table 2. In Table 2, we can see that the 9Cr-5Si-3Al alloys exhibit lower k_p values than the 9Cr-5Si alloys at both oxidation temperatures of 900 °C and 1000 °C. Therefore, low k_p values, we can conclude that the 9Cr-5Si-3Al alloy exhibits better oxidation resistance. This improvement in the oxidation properties can be attributed to the effect of the Al alloying element.

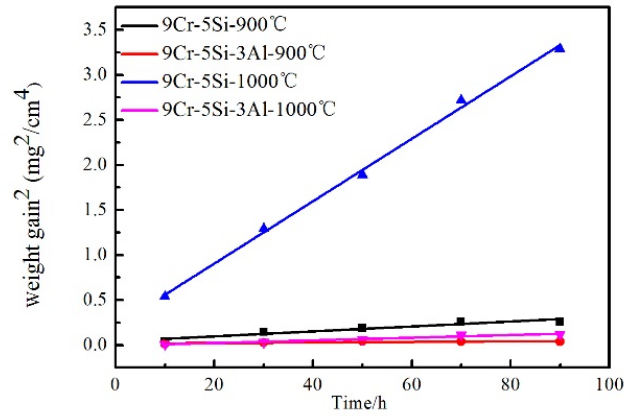


Fig. 2. $(\Delta W/A)^2$ versus t(h) plots of cyclic oxidation-kinetics curves of two alloys

Table 2. k_p values of the alloys at different temperatures/ $\text{mg}^2 \cdot \text{cm}^{-4} \cdot \text{h}^{-1}$

	900 °C	1000 °C
9Cr-5Si	2.75×10^{-3}	3.47×10^{-2}
9Cr-5Si-3Al	3.30×10^{-4}	1.48×10^{-3}

3.2. XRD characterization of the oxide layers

Fig. 3 shows the XRD patterns of both alloys after oxidation for 10h, 50h, and 90h at 900°C and 1000°C. In Fig. 3a, Cr_2O_3 and Cr_2MnO_4 phases can be identified after oxidation at 900°C to 1000°C at different times and the oxide content on the surface increases with increases in both the oxidation temperature and time. Furthermore, we find that the intensity of the α -Fe diffraction peak obviously decreases with increases in the oxidation time at 1000 °C, which contributed to

the increase in the thickness of the oxidation layer. However, at 900 °C the α -Fe diffraction peak shows no obvious change with increases in the oxidation time. This is most likely due to the low rate of growth of the oxide layer at 900 °C, which results in a thin oxide layer. As shown in Fig. 3b, the oxide layer of the alloy to which Al had been added exhibits an Al_2O_3 phase at both 900 °C and 1000 °C as well as an α -Fe matrix. After oxidation, no Cr_2O_3 or Cr_2MnO_4 phases are found in the 9Cr-5Si-3Al alloy, which indicates that the addition of Al changes the structure of the oxide film on the surface of the sample due to the high affinity of Al for oxygen. The formation of Al_2O_3 in the outer layer occurs prior to the formation of other oxides in steels.

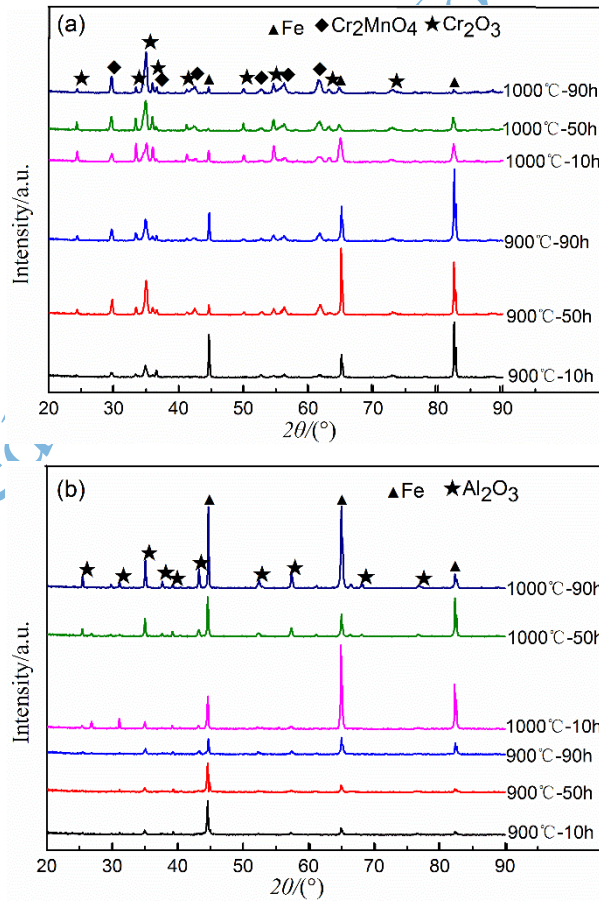


Fig. 3. XRD patterns of the alloys oxidized at various stages: (a) 9Cr-5Si, (b) 9Cr-5Si-3Al

3.3 Evolutions of the oxidation layer

Fig. 4 shows the surface morphologies of the oxides of the 9Cr-5Si alloy after oxidation at 900°C and 1000°C for 50h. As we can see in the figure, the surface morphology of the oxide exhibits regular polyhedral particles at oxidation temperatures of both 900°C and 1000°C. However, it is clear that the size of the oxide particles formed at 1000°C are larger than those formed at 900°C, and some small spherical particles can be seen in Fig. 4b.

The surface morphologies of the oxide of the 9Cr-5Si-3Al alloy oxidized at 900°C and 1000°C are shown in Figs. 5a and 5b, respectively, in which we can see that the oxides formed at an oxidation temperature of 900°C have a whisker-like shape and with increases in the oxidation time, the volume of whisker-like oxides increases, which results in full coverage of the sample surface. However, after oxidation at 1000 °C for 50h, the oxide particles exhibit a uniform polyhedral shape, as shown in Fig. 5c, and the whole surface of the sample is covered. The whisker-like oxides can be considered to be metastable θ -Al₂O₃ when oxidized at 900 °C which are then transformed into a stable and granular α -Al₂O₃ at 1000°C [24].

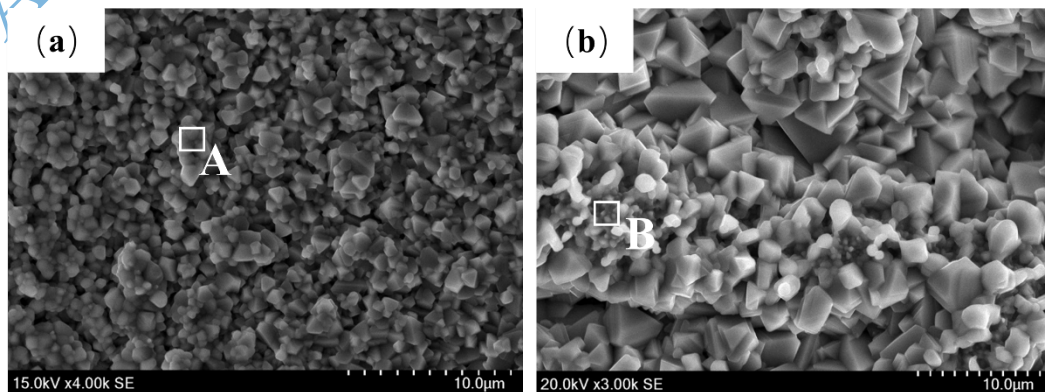


Fig. 4. SEM surface morphologies of 9Cr-5Si alloy at 900 °C for 50h, (b) at 1000 °C for 50h

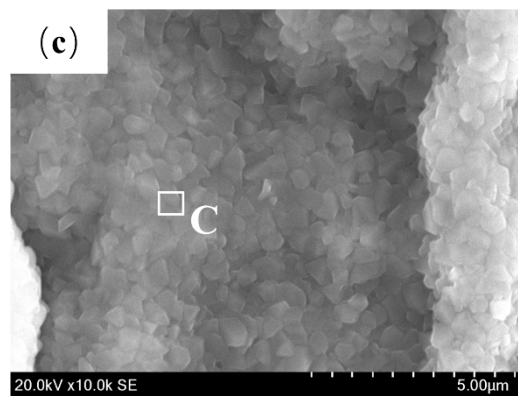
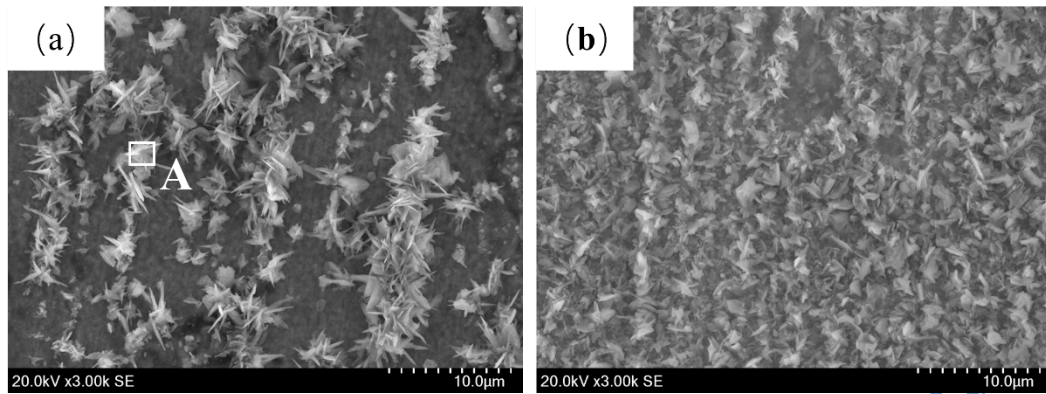


Fig. 5. SEM surface morphologies of 9Cr-5Si-3Al alloy at 900 °C for 50h

Tables 3 and 4 show the chemical compositions, as determined by EDS analysis, of the 9Cr-5Si and 9Cr-5Si-3Al alloys after oxidation at 900 °C and 1000 °C. The results indicate that the oxide particles of the 9Cr-5Si alloy contain higher O, Cr, and Mn contents, as shown in Table 3. Hence, we can conclude that the oxide particles are Cr_2MnO_4 and Cr_2O_3 . Table 4 shows the results obtained for the 9Cr-5Si-3Al alloy oxidized at 900 °C and 1000 °C, which clearly indicate that the oxides on the surface mainly contain O and Al after oxidation at 900 °C and 1000 °C, from which we can infer that these surface oxides exhibit an Al_2O_3 phase.

Table 3. Chemical composition of 9Cr-5Si alloy after oxidation at 900°C

Region	Atom fraction/%					
	O	C	Cr	Fe	Mn	Si
A	54.61	-	22.31	1.39	21.53	0.16
B	50.41	17.01	21.79	0.78	9.93	0.07

Table 4. Chemical composition of 9Cr-5Si-3Al alloy after oxidation at 1000°C

Region	Atom fraction/%				
	O	Cr	Fe	Al	Si
A	60.90	0.21	0.55	38.31	0.03
C	55.75	1.17	8.17	34.19	0.73

Fig. 6 shows the backscattered electron image (BSE) cross-sectional morphologies of the specimens after oxidation at 900°C and 1000°C for 90h, in which we can clearly see that the oxide layer of the 9Cr-5Si alloy is much thicker after oxidation at 1000°C than that at 900°C. However, the oxide layer of the 9Cr-5Si-3Al alloy is much thinner than that of 9Cr-5Si alloy for the same oxidation conditions and exhibits no obvious increase in thickness with an increase in temperature. These results indicate that the 9Cr-5Si-3Al alloy has a lower oxidation rate than the 9Cr-5Si alloy with an increase in the oxidation temperature, which results in better oxidation resistance even at the high temperature of 1000°C. This result also is consistent with the oxidation kinetics shown in Fig. 1 and confirms that the addition of Al serves to

improve the oxidation resistance of the alloy.

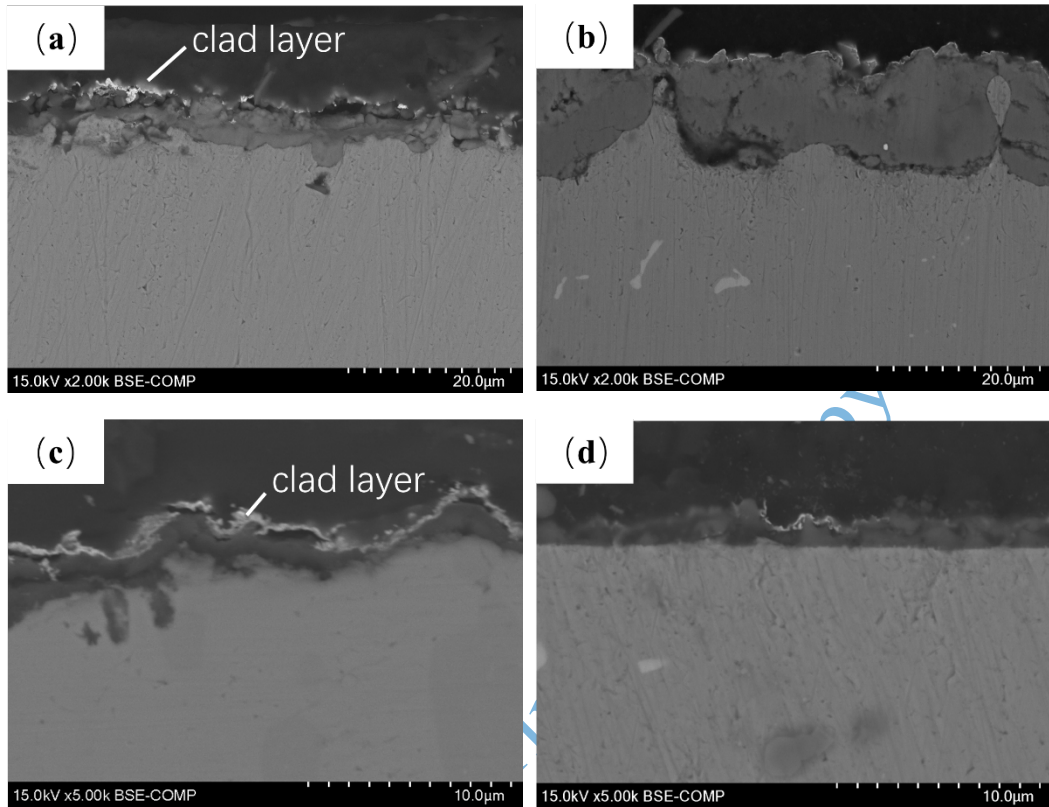
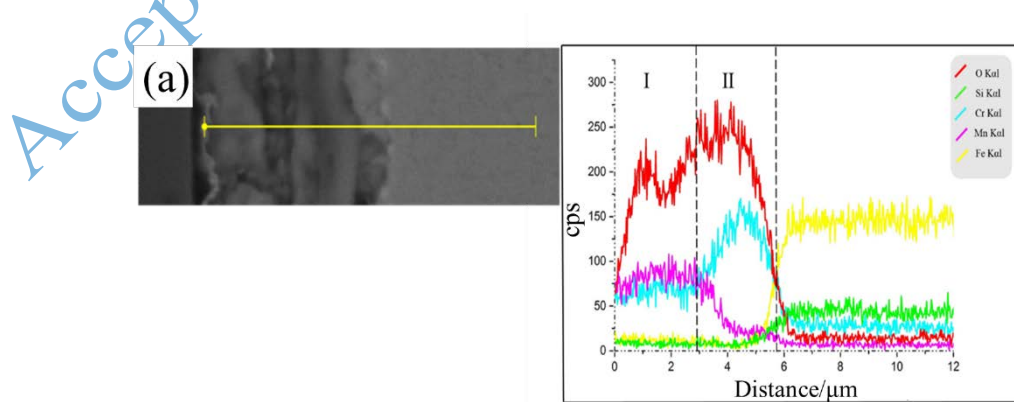


Fig. 6. BSE cross-sectional micrographs of 9Cr-5Si alloy and 9Cr-5Si-3Al alloy after oxidation, (a) and (b) 9Cr-5Si alloy at 900 °C and 1000 °C, (c) and (d) 9Cr-5Si-3Al alloy at 900 °C and 1000 °C



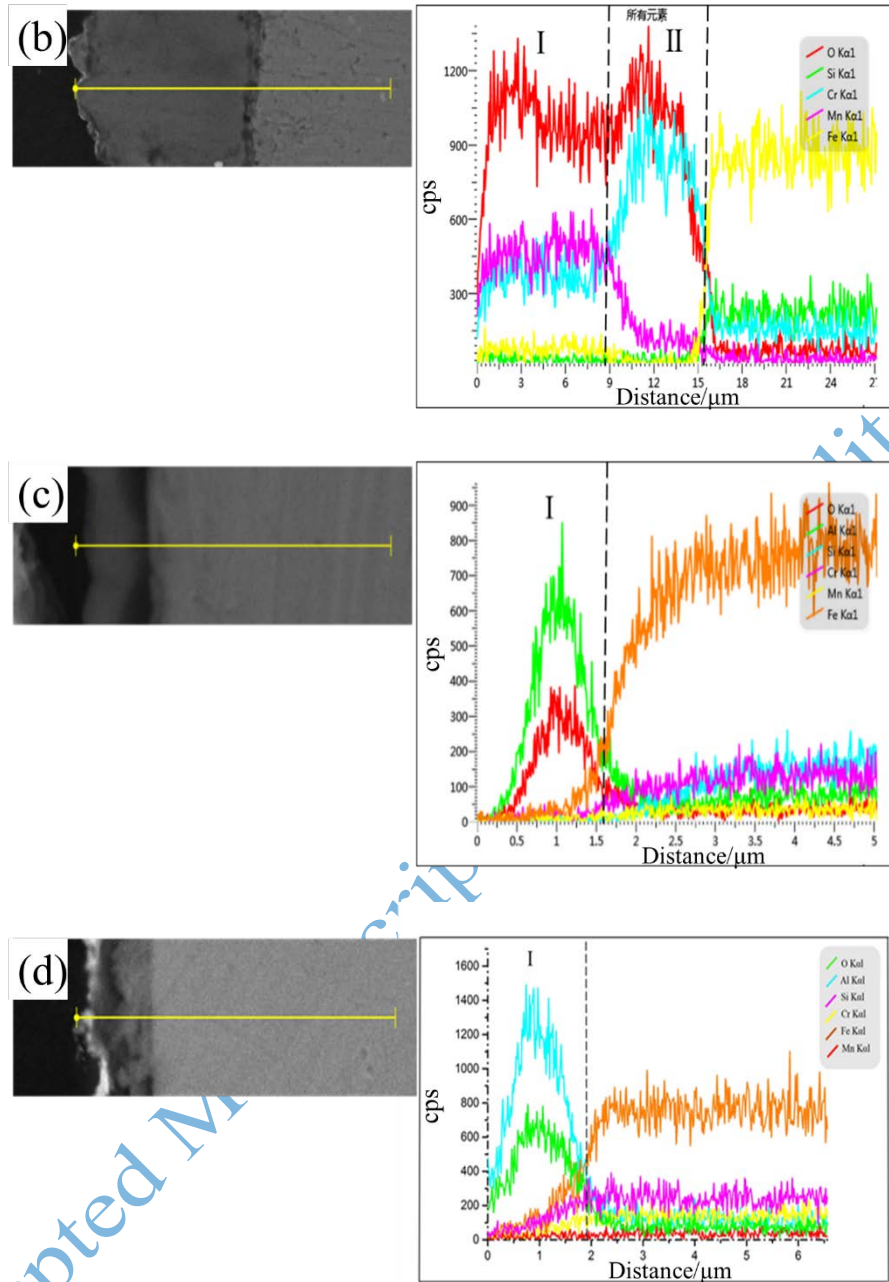


Fig. 7. EDS depth profiles of the alloys oxidized at 900°C and 1000°C for 90h: (a) and (b) 9Cr-5Si alloy at 900 °C and 1000 °C, respectively, (c) and (d) 9Cr-5Si-3Al alloy at 900 °C and 1000 °C, respectively.

Fig. 7 shows the element depth profiles of the 9Cr-5Si and 9Cr-5Si-3Al alloys by EDS line-scan analysis after oxidation at 900°C and 1000°C for 90h. As shown in Figs.7a–7b, the elements Mn and Cr are enriched in a range from the surface to about

3 μm and 9 μm after oxidation at 900

°C and 1000°C from 900

Mn content decreases and the Cr content increases significantly in the range from 3–6 and 9–15 μm , respectively. These results indicate that the oxide layer of the 9Cr-5Si alloy after oxidation at 900 °C at both 1000°C and 900°C consist Cr₂O₃ in the outer layer and only Cr₂O₃ in the inner layer. The results also indicate that the thickness of the oxide layer obviously increases with an increase in the oxidation temperature, which is consistent with the results shown in Fig. 6. As such, Mn obviously has good mobility through the lattice, since it was detected throughout and on top of the Cr₂O₃ layer. The formation of an MnCr₂O₄ outer layer can be attributed two main reasons, the first being that the high diffusivity of Mn²⁺ in the Cr₂O₃ layer promotes the outward diffusion of Mn²⁺ to the surface [24]. The second reason is that the MnO formed on the outward side of the oxide layer reacts with Cr₂O₃ to immediately form Cr₂MnO₄ spinel oxides due to the more negative standard Gibbs free energy associated with the formation of Cr₂MnO₄ oxides than with binary MnO and Cr₂O₃ oxides, which results in the Cr₂MnO₄ spinel phase being more stable [13, 24]. The reaction equation can be described as follows:



In addition, the MnCr₂O₄ spinel oxides act as a compact barrier to retard the inward diffusion of O, which reduces the weight gained by the oxide layer [25].

As shown in Figs. 7c–7d, only the O and Al are enriched from the surface to about 1.5–2 μm at oxidation temperatures of 900°C and 1000°C for the 9Cr-5Si-3Al alloy. This indicates that the oxide layer only consists of Al₂O₃ and is thinner than that

of the 9Cr-5Si alloy. Based on the Gibbs free energy associated with the formation of Al_2O_3 [26], Al has high affinity for oxygen, which results in the formation of Al_2O_3 in the outer layer prior to the formation of other oxides in steels. Once the Al_2O_3 layer has formed on the surface, the flux of oxygen from the outer layer to the inner layer is greatly decreased. Therefore, it is very difficult for other oxides to form, so the oxidation rate obviously decreases once the continuous and compact Al_2O_3 layer has formed on the surface of the steel. Thus, the oxidation resistance of the steels at high temperature is significantly improved.

4 Conclusions

In summary, the oxidation behaviors of the 9Cr-5Si and 9Cr-5Si-3Al ferritic heat-resistant steels are as follows:

(1) The oxidation-kinetics curves of the 9Cr-5Si and 9Cr-5Si-3Al ferritic heat-resistant steels were found to follow the parabolic law. The 9Cr-5Si-3Al steel exhibited lower oxidation rates than those of 9Cr-5Si steel at both 900°C and 1000°C, and its oxidation rate showed no significant increase with an increase in the oxidation temperature.

(2) The outer oxide layer of the 9Cr-5Si alloy exhibited MnCr_2O_4 and Cr_2O_3 phases after oxidation at 900 °C and 1000°C. However, only in the inner layer.

(3) The oxide layer of the 9Cr-5Si-3Al alloy consisted only of the Al_2O_3 phase at

oxidation temperatures of 900°C and 1000°C and this layer was much thinner than that of the 9Cr-5Si alloy. The Al₂O₃ oxide layer was continuous and compact on the surface of the steel, which indicates that the addition of Al in steel can significantly improve the high-temperature oxidation resistance of steels.

Acknowledgements

The authors acknowledge financial support from the Science & Technology Department of Sichuan Province, China (Grant No. 2017KJT0110).

References

- [1] Dae-Bum Park, Sung-Min Hong, Kyu-Ho Lee, Moo-Young Huh, Jin-Yoo Suh, Seung-Cheol Lee, and Woo-Sang Jung, High-temperature creep behavior and microstructural evolution of an 18Cr9Ni3CuNbVN austenitic stainless steel, *Mater. Charact.*, 93 (2014), p. 52.
- [2] Min-Ho Jang, Jun-Yun Kang, Jae Hoon Jang, Tae-Ho Lee, and Changhee Lee, Hot deformation behavior and microstructural evolution of alumina-forming austenitic heat-resistant steels during hot compression, *Mater. Charact.*, 123(2017), p. 207.
- [3] E. Huttunen-Saarivirta, V.T. Kuokkala, and P. Pohjanne, Thermally grown oxide films and corrosion performance of ferritic stainless steels under simulated exhaust gas condensate conditions, *Corros. Sci.*, 87(2014), p. 344.
- [4] Paul D. Jablonski and David E. Alman, Oxidation resistance of novel ferritic stainless steels alloyed with titanium for SOFC interconnect applications, *J. Power Sources*, 180(2008), p. 433.
- [5] D.Rojas, J.Garcia, O.Prat, G.Sauthoff, and A.R.Kaysser-Pyzalla, 9%Cr heat resistant steels: Alloy design, microstructure evolution and creep response at 650°C, *Mater. Sci. Eng. A*, 528(2011), p. 5164.
- [6] L.Tan, X.Ren and T.R. Allen, Corrosion behavior of 9 - 12% Cr ferritic - martensitic steels in supercritical water, *Corros. Sci.*, 52(2010), p. 1520.
- [7] X.S. Zhou, Y.C. Liu, C.X. Liu, and B.Q. Ning, Evolution of creep damage in a modified ferritic heat resistant steel with excellent short-term creep performance and its oxide layer characteristic, *Mater. Sci. Eng. A*, 608(2014), p. 46-52.
- [8] Y.P. Zeng, J.D. Jia, W.H. Cai, and S.Q. Dong, Effect of long-term service on the precipitates in P92 steel, *Int. J. Miner. Metall. Mater.*, 25(2018), No.8, p. 913.
- [9] C. Zhang, L. Cui, Y.C. Liu, C.X. Liu, and H.J. Li, Microstructures and mechanical properties of friction stir welds on 9% Cr reduced activation ferritic/martensitic steel, *J. Mater. Sci. Technol.*, 34(2018), No. 5, p. 756.
- [10] X.S. Zhou, C.X. Liu, L.M. Yu, Y.C. Liu, and H.J. Li, Phase Transformation Behavior and Microstructural Control of High-Cr Martensitic/Ferritic Heat-resistant Steels for Power and Nuclear Plants: A Review. *J. Mater. Sci. Technol.*, 31(2015), No. 3, p. 235.

-
- [11] Min-Ho Jang, Joonoh Moon, Jun-Yun Kang, Heon-Young Ha, Baig Gyu Choi, Tae-Ho Lee, and Changhee Lee, Effect of tungsten addition on high-temperature properties and microstructure of alumina-forming austenitic heat-resistant steels, *Mater. Sci. Eng. A*, 647(2015), p. 163.
- [12] J. Ren, L.M. Yu, Y.C. Liu, Z.Q. Ma, C.X. Liu, H.J. Li, and J.F. Wu, Corrosion behavior of an Al added high-Cr ODS steel in supercritical water at 600 °C, *Appl. Surf. Sci.*, 480(2019), p. 969.
- [13] D.N. Zou, Y.Q. Zhou, X. Zhang, W. Zhang, and Y. Han, High temperature oxidation behavior of a high Al-containing ferritic heat-resistant stainless steel, *Mater. Charact.*, 136 (2018), p. 435.
- [14] Y. L. Xu, X. Zhang, L. J. Fan, J. Li, X.J. Yu, and X.S. Xiao, Improved oxidation resistance of 15 wt.% Cr ferritic stainless steels containing 0.08 - 2.45 wt.% Al at 1000 °C in air, *Corros. Sci.*, 100(2015), p. 311.
- [15] Josip Brnic, Goran Turkal, Sanjin Krscanski, Domagoj Lanc, Marko Canadija, and Marino Brcic, Information relevant for the design of structure: Ferritic - Heat resistant high chromium steel X10CrAlSi25, *Mater. Des.*, 63(2014), p. 508.
- [16] C.Z. Lu, J.Y. Li, and Z. Fang, Effects of asymmetric rolling process on ridging resistance of ultra-purified 17%Cr ferritic stainless steel. *Int. J. Miner. Metall. Mater.*, 25(2018), No.2, p. 216.
- [17] H. Fujikawa and S.B. Newcomb, High Temperature Oxidation Behaviour of High Al Content Ferritic and Austenitic Stainless Steels With and Without Rare-Earth Element Addition, *Oxid. Met.*, 77(2012), p. 85.
- [18] L.L. Wei, L.Q. Chen, M.Y. Ma, H.L. Liu, and R.D.K. Misra, Oxidation behavior of ferritic stainless steels in simulated automotive exhaust gas containing 5 vol.% water vapor, *Mater. Chem. Phys.*, 205(2018), p. 508.
- [19] Gordon R. Holcomb and David E. Alman, The effect of manganese additions on the reactive evaporation of chromium in Ni - Cr alloys, *Scripta Mater.*, 54(2006), No.10, p. 1821.
- [20] J. Zurek, D.J. Yong, E. Essuman, M.Hansel, H.J. Penkalla, L. Niewolak, and W.J. Quadackers, Growth and adherence of chromia based surface scales on Ni-base alloys in high- and low-pO₂ gases, *Mater. Sci. Eng. A*, 477(2008), p. 259.
- [21] T.B. Gu, C.G. Yin, W.C. Ma, and G.Y. Chen, Municipal solid waste incineration in a packed bed: A comprehensive modeling study with experimental validation, *Appl. Energ.*, 247(2019), p. 127.
- [22] Y. Li, X.G. Zhao, Y.B. Li, and X.Y. Li, Waste incineration industry and development policies in China, *Waste Manage.*, 46(2015), p. 234.
- [23] Deepa Mudgal, Lalit Ahuja, Surendra Singh, Satya Prakash, Corrosion behaviour of Cr 3 C 2 -NiCr coated superalloys under actual medical waste incinerator, *Surf. Coat. Technol.*, 325(2017), p. 145.
- [24] Srinivasan Swaminathan, Young-Su Lee, and Dong-Ik Kim, Long term high temperature oxidation characteristics of La and Cu alloyed ferritic stainless steels for solid oxide fuel cell interconnects, *J. Power Sources*, 327(2016), p. 104.
- [25] Hadi Ebrahimifar, and Morteza Zandrahimi, Mn coating on AISI 430 ferritic stainless steel by pack cementation method for SOFC interconnect applications, *Solid State Ionics*, 183(2011), No, p. 71.
- [26] Deepa Mudgal, Lalit Ahuja, Divya Bhatia, Surendra Singh, and Satya Prakash, High temperature corrosion behaviour of superalloys under actual waste incinerator environment, *Eng. Fail. Anal.*, 63(2016), p. 160.

Accepted Manuscript Not Copyedited